Quantifying and correcting tilt-related positioning errors in microcantilever-based microelectromechanical systems probes

Steve Arscott

▶ **To cite this version:**

Steve Arscott. Quantifying and correcting tilt-related positioning errors in microcantilever-based microelectromechanical systems probes. Journal of Micromechanics and Microengineering, 2023, 32 (5), pp.057001. 10.1088/1361-6439/acd25e . hal-04092921

HAL Id: hal-04092921
https://hal.science/hal-04092921

Submitted on 11 May 2023

HAL is a multi-disciplinary open access archive for the deposit and dissemination of scientific research documents, whether they are published or not. The documents may come from teaching and research institutions in France or abroad, or from public or private research centers.

L'archive ouverte pluridisciplinaire **HAL**, est destinée au dépôt et à la diffusion de documents scientifiques de niveau recherche, publiés ou non, émanant des établissements d'enseignement et de recherche français ou étrangers, des laboratoires publics ou privés.

Quantifying and correcting tilt-related positioning errors in microcantilever-based microelectromechanical systems probes

Steve Arscott

University of Lille, CNRS, Centrale Lille, University Polytechnique Hauts-de-France, UMR 8520-IEMN, F-59000 Lille, France.

steve.arscott@univ-lille.fr

Abstract

The impact of tilt-related errors on the positioning of microcantilever-based microelectromechanical systems (MEMS) on-wafer electrical probes, having multiple contact pads, is quantified and investigated here. A tilt error associated with probe roll results in the probe contact pads not being parallel to the approaching surface as a downward overtravel is imposed—this leads to one probe pad making contact with the surface before the others. In a MEMS-based probe, the analysis of the impact of roll error angle must consider both the bending and the torsion of the flexible cantilever as the overtravel is increased—something which eventually results in all pads being in contact with the surface, but not with the same contact force. An original mathematical description of the problem is presented. By making some assumptions, the analytical modelling enables the derivation of elegant equations relating the roll error angle and the cantilever deflection to achieve planarity of the cantilever apex with the underlying surface. The modelling predicts probe tip planarity for rectangular and trapezoidal shaped probes. The predictions of the modelling are tested by using macroscopic cantilevers—excellent agreement between modelling and experiment is demonstrated. The macroscopic experimental setup reveals interesting behaviour concerning a bending/twisting, tilted cantilever in contact with—and skating across—an underlying surface. The experimental findings also indicate the pertinence of the modelling for the potential use with understanding the behaviour of microscopic cantilevers—such as MEMS-based probes—similarly in contact with a surface. A flexible microcantilever enables a torsional compensation of the roll error angle. It also enables a protocol where the roll error angle can be corrected. The design geometry of the probe tip will determine which approach is best suited. In principle, the modelling is scalable to MEMS probes composed of silicon-based cantilevers.

1. Introduction

Electrical test probes have been developed in some shape or form for a very long time. Since the 1970s, radio frequency (RF) probes have been developed to perform 'on-wafer' characterization of the fruits of the ongoing microelectronics revolution—both for analogue and digital devices and systems [1–3]. Indeed, as both the miniaturization and working frequency of microelectronics has evolved, so have electrical probes also evolved to maintain characterization performance—this has involved their own miniaturization. As probes and target contact pads on the wafer become smaller, probe placement becomes more challenging [4]. The manufacture of smaller probes also becomes more exigent [5], and traditional assembly-based fabrication may soon need to be replaced by micro and nanofabrication. In this important context, the impact of various position errors on the performance of high frequency electrical probes has been studied by a number of authors. Most of these studies concern the placement of macroscopic commercial probes [6]—where the potential mechanical flexibility of the probe was not considered. For example, the effect of in-wafer-plane probe position error on high frequency characterization performance has been studied [7,8]. Chen *et al* [9] concluded that the dominant error source of THz probes is indeed positioning. Position error involving very small signal lines has also been investigated [10], pointing to miniaturization position issues. In addition, the effect of roll error angle on the electrical properties of the rigid probe/contact pad high frequency behaviour has been studied [11,12]—with innovative solutions being proposed [13,14].

In terms of miniature probes, automatic positioning to avoid errors has been studied [15–17]. Quantifying and controlling tilt errors is essential for optimised automated probing using microcantilevers. However, the latter studies did not take into account the mechanical flexibility of miniature, potentially MEMS-based, probes. Microcantilevers can be used to make all manners of miniaturized electrical probes, including RF probes [18–21]. Microcantilevers are fabricated using microelectromechanical systems (MEMS) fabrication techniques—this enables probes to be small, mechanically flexible, and compatible with the incorporation, at the fabrication stage, of microelectronics' materials and devices. However, the inherent mechanical flexibility of a microcantilever needs to be considered for optimum probing and electrical contacting. In terms of microcantilever-based probes, the impact of mechanical flexibility on the probe positioning has been described by the author for probes based on both flexible rectangular [22] and triangular microcantilevers [23]. Indeed, tip skate itself can be regarded as a positioning error—something that can be, in principle, eliminated using skate compensation [22]. The overtravel/skate/contact force relationship of such probes was fully described. This analysis resulted in a basic easy-to-use modelling toolbox. However, the analysis ignored the effect of potential tilt-related geometrical position errors on the tip-surface contacting of such probes—something often encountered in practice.

In the case of miniature RF probes, three electrical contacts are required: e.g. a signal contact surrounded by two ground contacts—this is true for both coplanar waveguide (CPW) and microstrip configurations. The central signal contact is separated from the adjacent ground contacts by a distance defined by the microwave design—this separation means that the probe tip has a finite apex length (in contrast to, for example, an atomic force microscopy (AFM) probe point). For optimal electrical contacting, these three contacts must all be simultaneously in intimate contact with the underlying test feature—usually metallic contact pads, lithographically defined on the underlying surface. A sufficient contact force must also be present to enable a low resistance electrical contact. Given this microcantilever-based probe configuration, let us now look at sources of placement error and see if we can quantify them.

2. Definition of pitch, yaw, and roll errors in microcantilever-based electrical probes

Let us consider Figure 1. Fig.1(a) shows the three principal axes of rotation of a probe based on a microcantilever—one can borrow the analogy from aircraft positioning. The 'pitch error', shown in Fig. 1(b), results from an error in—what is commonly known as—the tilt angle $\Delta\theta$ of the probe. The 'yaw error', shown in Fig. 1(c), results form a rotation of the probe whilst maintaining the apex edge of the cantilever parallel to the underlying surface; the angle β is in the plane of the surface. The probe tip edge is not *perpendicular* to a target feature on the surface—this is a visible *alignment problem*. In contrast, the 'roll error', shown in Fig. 1(d), originates from a rotation of the probe whereby the edge of the apex of the cantilever is not parallel with the underlying surface. In this case, one corner of the end of the cantilever is not in contact with the surface upon touchdown; note that the angle φ is perpendicular to the cantilever—see Supplementary Information.

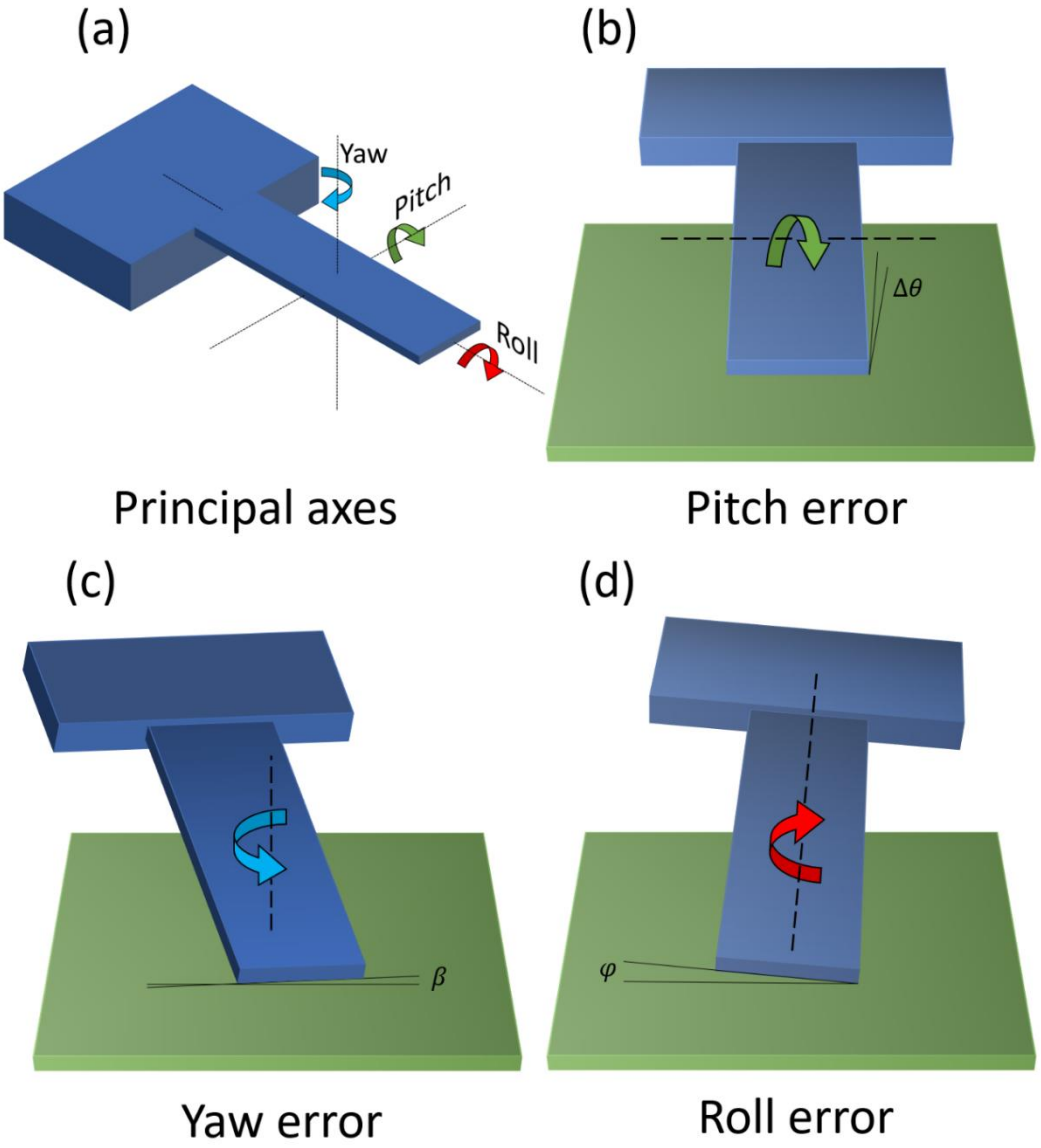

Figure 1. The principle axes of a microelectromechanical systems (MEMS) microcantilever-based probe and the three potential sources of positioning error associated with these axes. (a) The principal axes of rotation: pitch, yaw, and roll. (b) Pitch error, (c) yaw error, and (d) roll error.

Let us now talk about the consequences of these errors. First, the pitch error can influence the skating and the contact force of the probe. Second, the visible yaw alignment error is easily corrected by rotation of the surface or the probe to enable alignment—this will not be discussed here. The roll error is more complicated as, upon lowering the probe, one corner of the probe tip edge will contact the surface before the other corner. Roll error angle in small probes can be caused by several factors including non-planar probes (intrinsic mechanical stresses, fabrication issues), probe mounting precision—this is especially true if manual intervention is part of the assembly protocol, cleanliness (debris, dust), and probe holder imperfections and imprecisions (mechanical play).

A common practical solution to correct roll error angle with macroscopic probes is to lower the probe using excess overtravel, this causes visible skate marks (damage) on contact pad metallization present on the surface which are uneven in the presence of roll error. The action is repeated until the damage is visibly symmetric. For relatively robust macroscopic probes landing on large pads, this technique is acceptable—and damage to contact pads is tolerated. However, for miniaturized probes this method could significantly damage small contacts (both on the probe and on the wafer) and, in addition, be problematic from an observational point of view—something the author has experience in [20]. Here, I try to quantify the roll error for a flexible cantilever-based probe to enable the prediction of its impact on the overtravel/skate/contact force relationship of such probes. In doing so, probe designers have a modelling toolbox to quantify and predict the impact of roll error angle—and perhaps potentially-damaging practical trial and error methods during testing could be avoided for valuable probes.

3. Description of the problem

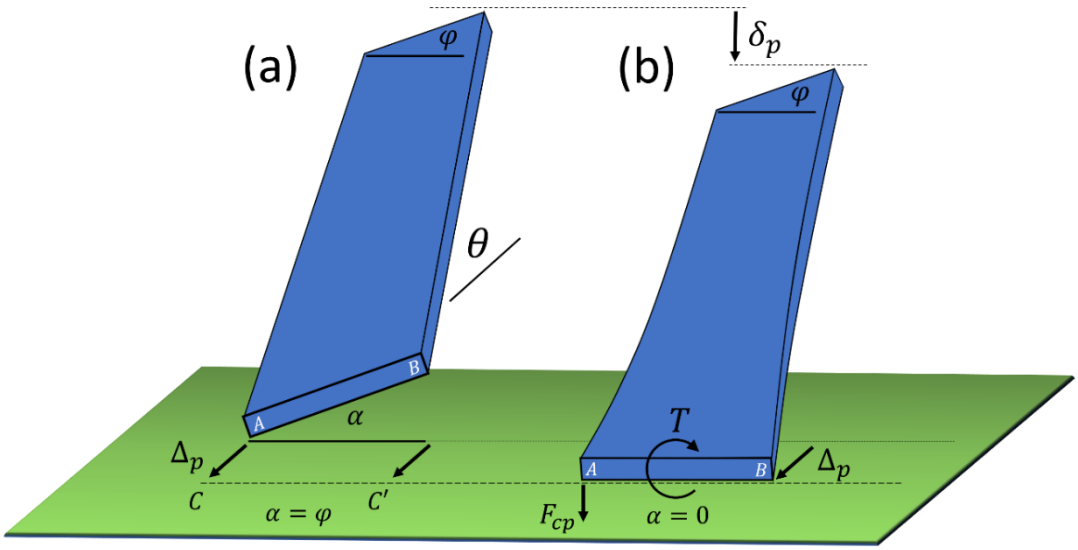

Figure 2. Schematic Illustration of roll error angle in a flexible microcantilever-based MEMS probe. (a) Touchdown and (b) apex planarity. The bending and torsion of the microcantilever are considered.

Let us consider Figure 2. We begin with an inclined, straight rectangular cantilever which is tilted at an angle θ relative to the flat surface and has a roll error angle of φ—see Fig. 2(a). An overtravel has been

applied until one corner of the cantilever (point A) comes into contact with the surface. At this point the apex angle α equals the roll error angle φ. If further overtravel is applied, two things occur. First, the corner A of the probe will skate over the surface—this is due to bending of the cantilever along the direction of its length. Second, a torque will cause twisting and warping of the cantilever. The apex angle α at the end of the cantilever will reduce—eventually bringing the opposite corner B of the end of the cantilever nearer the surface—see Fig. 2(b). When the apex angle α is zero, the points A and B will have reached points C and C' on the surface. The overtravel required to do this can be defined as the 'planarity overtravel' δ_p and the resulting skate the 'planarity skate' Δ_p. At apex planarity, the planarity contact force at point C on the surface is F_{cp}, at point C' it is zero. At this point, we can increase the overtravel further to increase the contact force beyond zero on corner B. If we do this, further tip skating will occur.

In terms of the contact force, three distinct phases occur as the overtravel is increased once the lower corner A of the cantilever tip edge is in contact with the surface. First, before planarity is achieved, the contact force between the lower contacting corner A and the surface increases—this is due to bending of the cantilever. This bending force cause torsion of the cantilever. At the precise overtravel required for planarity δ_p, the whole lower edge of the tip is in contact with the surface. At this point, the force varies linearly along the edge to zero at the other corner B. If the overtravel is increased beyond this, the extra bending of the cantilever will generate a force along the whole of the edge of the cantilever in contact with the surface. The contact force at opposite corner will thus increase. The force increases linearly along the whole edge of the cantilever which is now in contact (parallel to) with the surface.

We can therefore ask ourselves the following questions: For a given set of practical parameters (cantilever shape (e.g. rectangular, trapezoidal…), cantilever dimensions, elastic modulus, shear modulus, tilt angle, roll error angle), what overtravel is required to achieve tip planarity with the surface? What is the resulting planarity tip skate? What is the planarity contact force of the tip of the cantilever? For a given roll error, what overtravel needs to be imposed to achieve a certain contact force on the upper, initially-higher, corner B? The latter issue is important if there are several spatially-separated electrical contacts present on the tip. First, planarity is essential for all pads to be in physical contact with the surface. Second, a certain contact force may be necessary to achieve a minimum contact (metal-to-metal) resistivity. Let us now develop a simple model to predict this behaviour and provide a simple-to-use modelling toolbox for the engineer.

4. Modelling

Let us first consider a rectangular cantilever (length L, width w, and thickness t) having an elastic modulus E, a Poisson's ratio ν, and a shear modulus G. We assume that the cantilever is tilted (pitch) at an angle θ relative to a flat surface. In terms of friction, forward and lateral skate of the apex corner will occur according to the probe tilt angle θ and the friction coefficient μ of the two material making up the tip and the surface [22]: the corner of the apex skates if $\tan\theta > \mu$. We assume that the cantilever has a roll error angle φ. The angle the apex makes with the surface is initially α; this angle varies from φ to zero with torsion. The starting point for the modelling is when the lowest corner of the cantilever contacts the underlying surface. At this point there is no bending or torsion warping of the cantilever. Following this, we apply a vertical downward overtravel δ to the cantilever. The effect of this is to cause the tip of the cantilever to skate a distance Δ across the surface, with the lower corner of the edge of the cantilever in contact with the surface. The cantilever now begins twisting, with a torque T generated at the corner in contact with the surface.

To obtain a simple, approximate analytical model of the system some assumptions can be made. First, the bending cantilever can be modelled by a solution of the Euler-Bernoulli equation [24]. Second, the roll error angle φ is considered to be small <10° [12–14], such that the torque acting on the corner of the end edge of the cantilever is considered parallel with the contact force which causes the cantilever to deflect. Third, the cantilever only bends in the axial direction, there is no bending of the cantilever in the transverse direction—only warping—as we consider the transverse stiffness to be much greater than the axial/longitudinal direction stiffness. This means that as the torque increases due to the axial bending of the cantilever; the end edge (apex) of the cantilever (width w) remains straight and does not curve.

The value of torque required to twist the cantilever end by the apex angle α is given by:

$$T = \frac{GJ_{rect}\alpha}{L} \tag{1}$$

Where J_{rect} is the torsion constant of the rectangular cantilever. For a rectangular cantilever of uniform section, the torsion constant is given by [25]:

$$J_{rect} = wt^3\left[\frac{1}{3} - 0.21\frac{t}{w}\left(1 - \frac{t^4}{12w^4}\right)\right] \tag{2}$$

The torque force F_T (orthogonal to the lower end edge of the cantilever) at the corner of the cantilever in contact with the surface is given by:

$$F_T = \frac{2T}{w} \tag{3}$$

But we also know for a rectangular cantilever that the force F_C concentrated at the load required to obtain a certain cantilever deflection δ_y is given by [22]:

$$F_C = \frac{\delta_y E w t^3}{4L^3} \tag{5}$$

We can assume that F_T equals F_c for small roll error angles (e.g. $\cos 10 = 0.985$); therefore, the deflection of the tip (due to bending) required to achieve tip planarity δ_y^p, i.e. $\alpha = 0$ in Fig. 2, is given by:

$$\delta_y^p = \frac{8GJ_{rect}\varphi L^2}{w^2 E t^3} \tag{6}$$

Also, we know that the ratio between the shear and the elastic moduli is given by:

$$\frac{G}{E} = \frac{1}{2(1+\nu)} \tag{7}$$

Where ν is the Poisson's ratio. Therefore, we can write:

$$\delta_y^p = \frac{4L^2 J_{rect}\varphi}{(1+\nu)w^2 t^3} \tag{8}$$

Interestingly, the deflection required for apex planarity of a tilted rectangular cantilever is independent of the absolute values of the elastic and shear moduli—only depending on cantilever dimensions and the Poisson's ratio of the material.

However, we also know that the tip deflection is related to the vertical overtravel δ in the following way [22]:

$$\delta = \delta_y \cos\theta + \delta_x \sin\theta \tag{9}$$

$$\Delta = \delta \tan\theta - \frac{\delta_x}{\cos\theta} \tag{10}$$

where Δ is the tip skate and that the vertical δ_y and lateral δ_x movements of the tip due to bending are related by the following formula [22]:

$$\delta_x = fL\left[\sqrt{\frac{\sin^{-1}\frac{\delta_y}{L}}{\frac{\delta_y}{L}}} - 1\right] \tag{11}$$

where f is a constant equal to 7.4 for a rectangular cantilever bending according to a cubic polynomial solution. Therefore, as the planarity tip overtravel δ_p is a function of the tip y displacement δ_y^p, i.e. $\delta_p = g(\delta_y^p)$, then the roll error angle can be computed using:

$$\varphi = \frac{(1+\nu)w^2 t^3}{4L^2 J_{rect} g^{-1}(\delta_p)} \tag{12}$$

The above equation means that the roll error angle φ can be computed using a measurement of the planarity overtravel δ_p. By knowing δ_p, δ_y^p can be found—enabling the value of φ to be found.

Along with rectangular cantilevers, triangular-shaped trapezoidal probe shapes are also a common shape for probes. Let us now consider a flat trapezoidal cantilever having a uniform thickness t, a base width b, and apex length a.

For a trapezoidal cantilever the force F_C, concentrated at the load, required to obtain a certain deflection δ_y is given by [23]:

$$F_c = \frac{\delta_y E t^3}{6L^3}\left[\left(\frac{b^2+5a^2+6ab}{b^3+a^3+5ab^2+5a^2b}\right) - \left(\frac{2a}{4ab+b^2+a^2}\right)\right]^{-1} \tag{13}$$

As with the rectangular cantilever, the mechanical properties are E, ν, and G. The width w of the trapezoidal cantilever varies according to:

$$w(x) = \left(\frac{a-b}{L}\right)x + b \tag{14}$$

At the end of the cantilever, the torque force is given by:

$$F_T = \frac{2T}{a} \tag{15}$$

We can consider the torque T along the length of the cantilever to be constant. By making the assumption that the torsional constant varies along the length of the cantilever, the angle of twist α for a given torque T at the apex can be computed using:

$$\alpha = \frac{T}{G}\int_0^L \frac{1}{J(x)}dx \tag{16}$$

The torsion constant of a trapezoidal cantilever (non-uniform section) can be computed using the following relationship:

$$J_{trap} = L\left(\int_0^L \frac{1}{J(x)}dx\right)^{-1} \tag{17}$$

The last two equations can be solved numerically. Therefore, at apex planarity, the deflection δ_y^p required to cause planarity of the end of a trapezoidal cantilever is given by:

$$\delta_y^p = \frac{12L^2 G J_{trap}\varphi}{Et^3 a}\left[\left(\frac{b^2+5a^2+6ab}{b^3+a^3+5ab^2+5a^2b}\right) - \left(\frac{2a}{4ab+b^2+a^2}\right)\right] \tag{18}$$

Note that setting $a = b = w$, and $J_{trap} = J_{rect}$, one reverts back to the purely rectangular cantilever case.

As above we can therefore write:

$$\delta_y^p = \frac{6L^2 J_{trap}\varphi}{(1+\nu)t^3 a}\left[\left(\frac{b^2+5a^2+6ab}{b^3+a^3+5ab^2+5a^2b}\right)-\left(\frac{2a}{4ab+b^2+a^2}\right)\right] \quad (19)$$

Again, as is the case for a rectangular cantilever, for a trapezoidal cantilever the deflection required for apex planarity with the surface is independent of the absolute values of the elastic and shear moduli, and only depends on the Poisson's ratio. As the relationship between the apex deflection and the overtravel is known [22,23] by using Eq. 9 and Eq. 11 above, it is possible to compute the roll error angle from the measured overtravel causing planarity.

$$\varphi = \frac{(1+\nu)t^3 a}{6L^2 J_{trap} g^{-1}(\delta_p)}\left[\left(\frac{b^2+5a^2+6ab}{b^3+a^3+5ab^2+5a^2b}\right)-\left(\frac{2a}{4ab+b^2+a^2}\right)\right]^{-1} \quad (20)$$

We now have a useful tool box of equations to solve the problem and make some predictions about practical examples of probes where roll error may be present. The following section presents experimental work to test the modelling.

5. Experimental

5.1 Fabrication of cantilevers

Rectangular and trapezoidal shaped cantilevers were fabricated for the study using thin, dense polystyrene sheets measuring 200×300 mm (Schulcz GmbH, Germany) and having a nominal thickness of 1.5 mm. The details of the fabrication methods can be found in a previous publication [23]. As the elastic modulus of dense polystyrene [23] is approximately 100 times less than that of crystalline silicon in the <110> directions [26], the stiffness of centimetre-sized polystyrene cantilevers is of the same order as the stiffness of micrometre-sized silicon cantilevers. Therefore, macroscopic experimental results obtained using dense polystyrene can be used to test mechanical models and also give insights into the mechanical behaviour expected when using silicon-based microcantilevers.

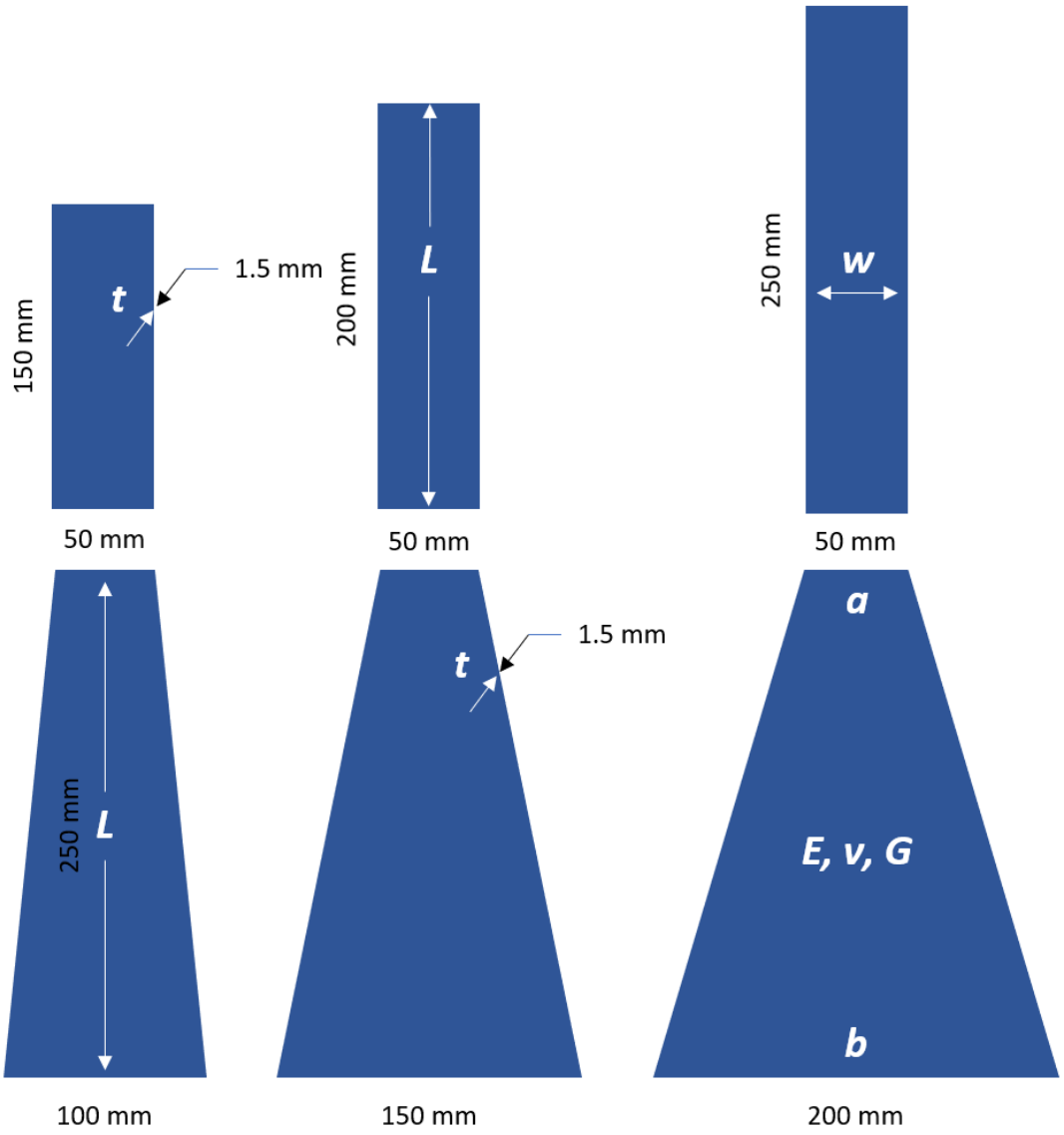

Figure 3. Dimension of the six dense polystyrene cantilevers fabricated for the experimental part of the study. (upper images) Rectangular cantilevers having different lengths: L = 150 mm, 200 mm, and 250 mm, decreasing in mechanical stiffness. (lower images). Trapezoidal cantilevers having different base widths: b = 100 mm, 150 mm, and 200 mm, increasing in mechanical stiffness. All cantilevers have a length of 250 mm and a nominal thickness t of 1.5 mm. The polystyrene mechanical properties relevant to the study are its elastic modulus E, its Poisson's ratio ν, and its shear modulus G.

A schematic diagram of the cantilever dimensions used for the experimental part of the study is shown in Figure 3. The fabrication techniques enabled the cantilever dimensions to be produced with relatively good accuracy. The lateral cutting accuracy was estimated to be ±0.5mm. As the smallest lateral dimension of the cantilevers is 50 mm, this corresponds to an accuracy of 1%. The

thickness of the polystyrene sheets was determined using a commercial precision thickness gauge (Mitutoyo, Japan) to be 1.515±0.012 mm.

5.2 Contact planarity overtravel and skate versus roll error

Figure 4 shows a schematic diagram of the experimental setup used to investigate the relationship between the planarity overtravel and skate versus the roll error angle. The cantilever (dark blue) was attached to a stable mechanical part (black) which could slide on a level surface (grey) to simulate the overtravel. The mechanical part enabled the cantilever to be oriented at 25° relative to the vertical surface (green)—this is the tilt angle θ of the cantilever. The cantilevers were attached to the mechanical part using stiff copper strips and G-clamps. The approach angle of the mechanical part could be varied to simulate a roll error angle φ. The skate and overtravel were measured using professional steel rulers allowing the measurement precision to be evaluated to be (±0.25 mm). For a typical overtravel of 50 mm, this corresponds to <1% measurement error. Note that gravity caused a slight of bending of the suspended cantilevers in the experimental setup—this was identified as the largest potential source of error in the measurements. This error was eliminated by making sure that the cantilever was perfectly straight (zero bending) at zero overtravel. A digital camera positioned directly above the end of the cantilever enabled both the roll error angle to be verified and for the moment of apex planarity to be determined. For a given roll error angle (1-3° were used in the current study), the overtravel was increased until contact planarity was observed. At this point, the planarity overtravel and skate were recorded for each cantilever. The experiments were performed several times to ensure measurement repeatability.

Note that the precise roll angle was obtained experimentally for each experiment. The precise roll angle for a specific set-up was evaluated from the photographic data. The apparent angle η the apex makes with the surface upon touchdown, when observing the apex of the cantilever using a camera that is inclined at an angle ω, is related to the probe tilt angle θ and the roll error angle φ by the relationship $\varphi = \eta/\cos(\theta + \omega)$. The apparent angle η is measured in the experiments using photography, thus enabling a precise measurement of the roll error angle in the experimental setups—the method for this is given in the Supplementary Information.

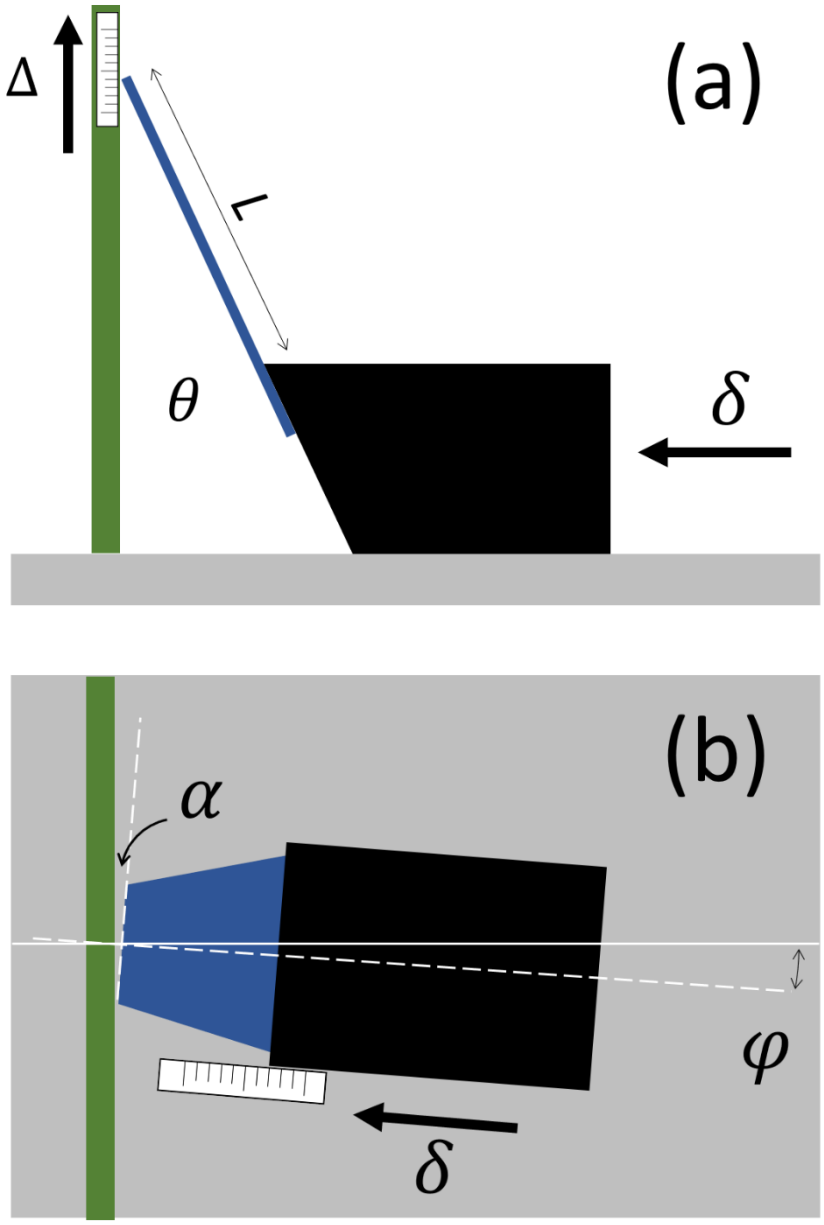

Figure 4. Schematic diagram of experimental setup used to determine the contact planarity overtravel and skate versus roll error angle φ. (a) Side view and (b) plan view. The black arrows indicate the direction of the overtravel δ. The cantilever (dark blue) is mounted on a sliding mechanical part (black). At touchdown $\alpha = \varphi$. The planarity skate Δ_p and planarity overtravel δ_p are recorded using precision rulers when torsion of the cantilever results in $\alpha = 0$.

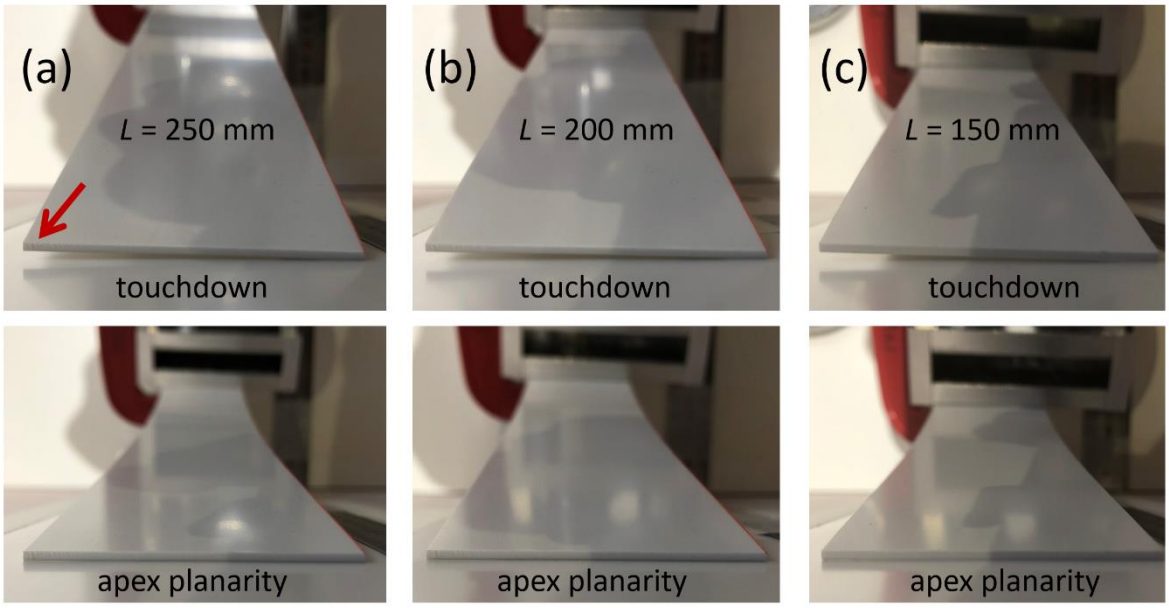

Figure 5. Examples of contact planarity experimental results for the rectangular cantilevers. Photographs of cantilever having a roll error angle of 2° in touchdown (upper images) and in apex planarity (lower images) for cantilevers having a length L of (a) 250 mm, (b) 200 mm, (c) 150 mm. The width of the rectangular cantilevers measures 50 mm and their thickness is 1.5 mm. The red arrow indicates the apparent roll error angle η which is related to the roll error angle φ, see Supplementary Information.

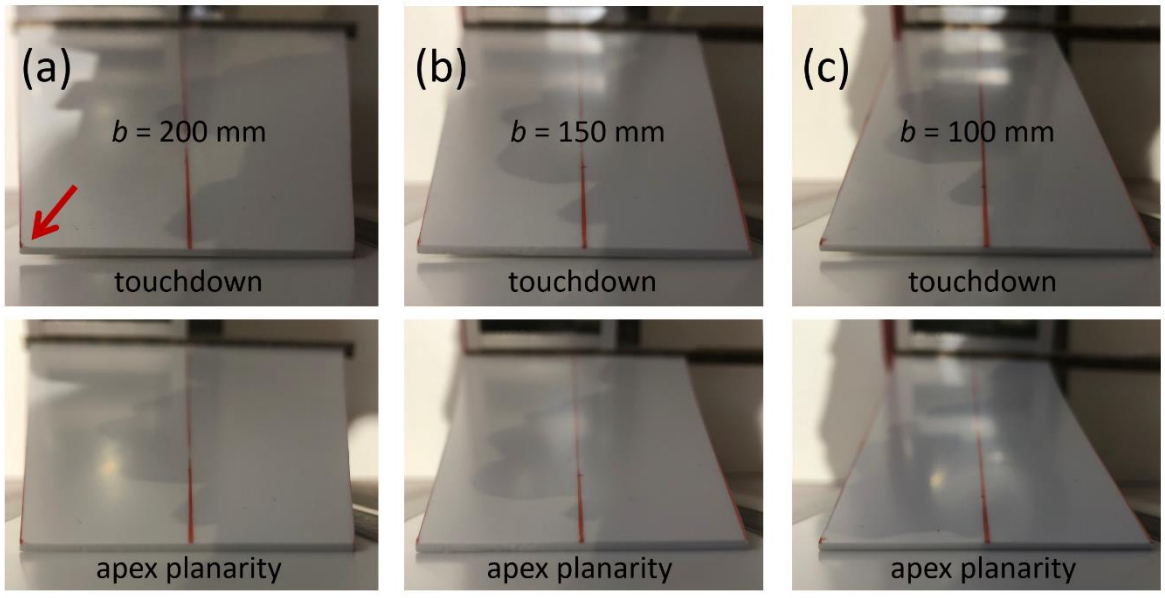

Figure 6. Examples of contact planarity experimental results for the trapezoidal cantilevers. Photographs of cantilever having a roll error angle of 1 degree in touchdown (upper images) and in apex planarity (lower images) for cantilevers having a base width b of (a) 200 mm, (b) 150 mm, (c) 100 mm. The apex of the trapezoidal cantilevers measures 50 mm and their thickness is 1.5 mm. The red arrow indicates the apparent roll error angle η which is related to the roll error angle φ, see Supplementary Information.

Figure 5 and Figure 6 show example photographs of the experimental results of the rectangular cantilevers—Fig. 5—and the trapezoidal cantilever—Fig.6. Each cantilever was initially brought into contact with the surface (upper images) and an overtravel is imposed until apex planarity was observed (lower images).

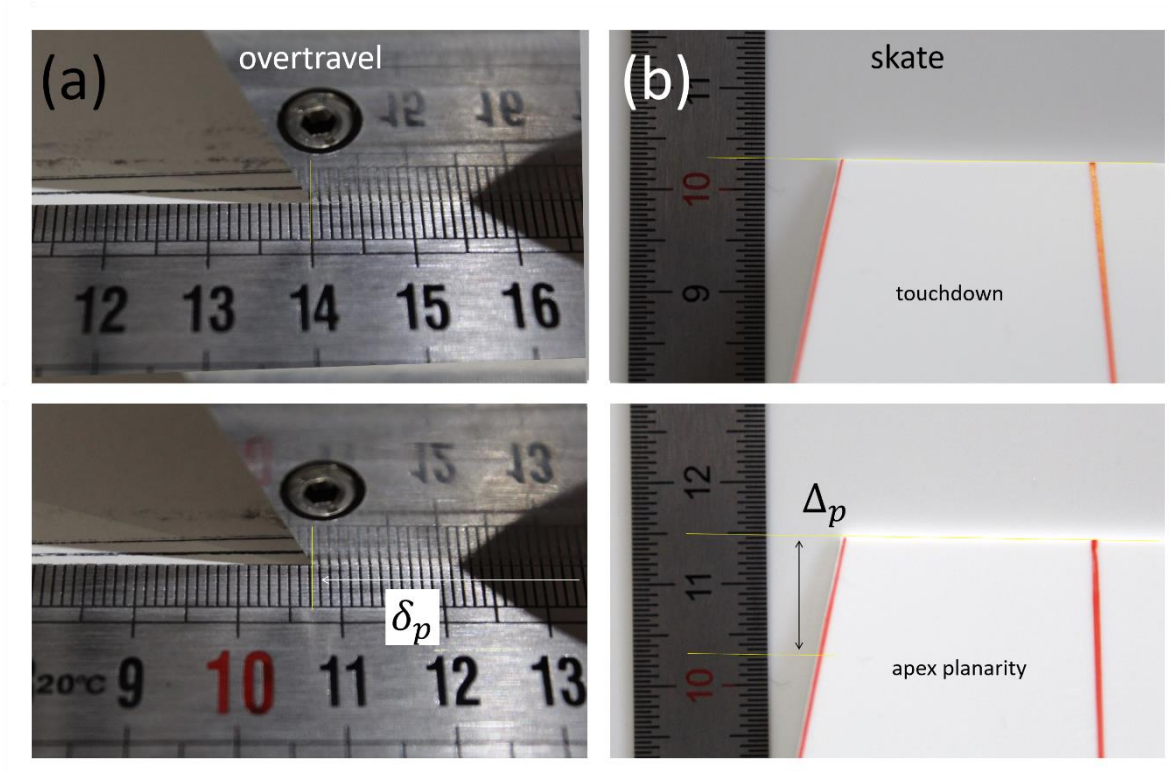

Figure 7. Examples of the measurement of the overtravel and the skate at apex planarity. (a) overtravel and (b) skate for a trapezoidal cantilever having a base b of 150 mm. The roll error angle φ = 3°, θ = 25°, a = 50 mm, L = 250 mm, and t = 1.515 mm.

Figure 7 shows photographs of how the planarity overtravel and skate were experimentally-evaluated. The upper images are taken at cantilever touchdown, the lower images are taken at apex planarity. The white arrow in the lower image of Fig. 7(a) indicates the overtravel direction. The black arrow in the lower image of Fig. 7(b) indicates the planarity skate. For the example given, the intended roll error angle is 2° and measured to be 2.18°. The planarity overtravel in this case is 32.75 mm, and the planarity skate is 11.75 mm.

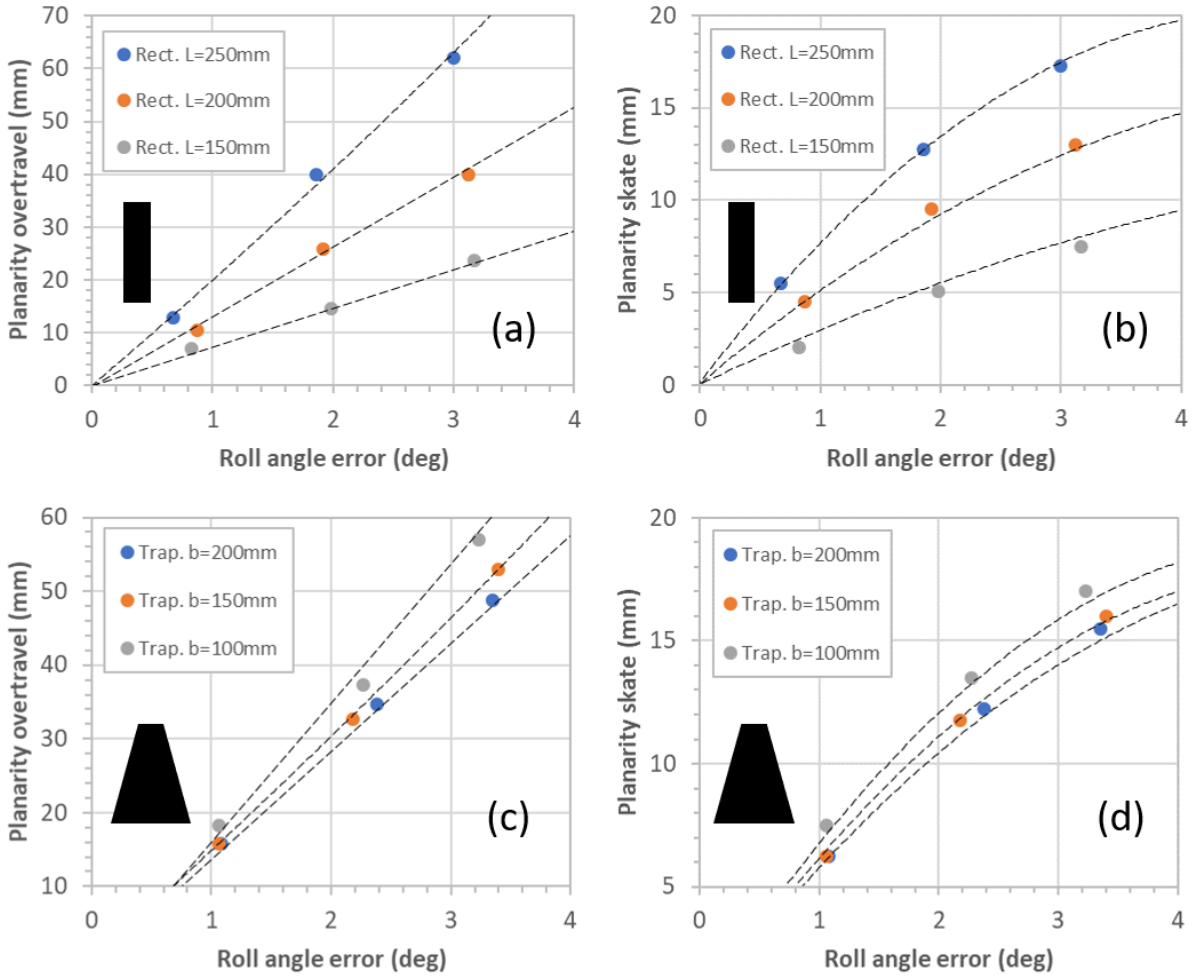

Figure 8. Planarity overtravel and skate as a function of roll error angle: comparison of experimental results (solid circles) with modelling (dashed lines). (a) and (b) Planarity overtravel and skate of rectangular cantilevers of varying length L. (c) and (d) Planarity overtravel and skate of trapezoidal cantilevers of varying base width b.

Figure 8 shows plots of the experimental results (solid circles) and compares them to results of the modelling (dashed lines). There are a number of observations we can make.

Let us first consider the rectangular cantilevers. With reference to Fig. 8(a), for a given length L, the overtravel required to obtain apex planarity increases with roll angle. For a shorter (stiffer) cantilever, the overtravel required for planarity is less for a given roll angle. For a given cantilever length, the planarity overtravel versus roll angle appears to be linear. With reference to Fig. 8(b), the experimental planarity skate increases with decreasing cantilever base width. The planarity skate also increases with increasing roll error angle. However, the relationships do not appear to be linear.

Let us now consider the trapezoidal cantilevers. With reference to Fig. 8(c), for a given base width b, the overtravel required to obtain apex planarity increases with roll angle. Second, for a wider-base (stiffer) cantilever, the overtravel required for planarity is less for a given roll angle. For a given cantilever base width, the planarity overtravel versus roll angle appears to be linear. With reference to Fig. 8(d), the experimental planarity skate increases with decreasing cantilever base width. The planarity skate also increases with increasing roll error angle. However, the relationships do not appear to be linear.

In all cases the modelling (the dashed lines in Fig. 8) fits the experimental data very well. All numerical values of this part of the study (experimental and the results of the modelling) can be found in the Supplementary information.

Finally, perhaps somewhat counterintuitively, the observations demonstrate clearly that a stiffer cantilever requires less overtravel to achieve tip planarity than a more flexible cantilever. This is because for a stiff cantilever, a higher contact force is generated at the contact point for a given overtravel compared to more flexible cantilever. This higher contact force leads to a higher torque, leading to greater torsion and thus obtention of planarity for less overtravel compared to a more flexible cantilever, i.e. a longer rectangular cantilever or a shorter-base trapezoidal cantilever.

5.3 Contact force and roll error

Figure 9 shows the schematic diagram of the experimental setup used to investigate the relationship between the contact force of the cantilevers and the surface as a function of roll error angle. A precision laboratory scales (Sauter GMbH, Germany) having a precision of ±0.1 g (i.e. ±981 µN) was employed to determine the contact force. The cantilever (dark blue) was oriented at a tilt angle θ of 25° relative to the surface of the adjustable laboratory table (orange) using a rigid mechanical part (black) attached to a laboratory stand (light blue). A layer of polystyrene sheeting (green) was used as the contact surface to minimize friction during tip skating. The friction coefficient of dense polystyrene on dense polystyrene is reported to be 0.35 [27]; the condition for tip skating [22] is therefore met. As

above, gravity causes a slight amount of bending of the cantilevers and is again certainly the largest potential source of error in the measurements—this is accounted for by making sure the cantilever is perfectly straight (zero bending) and oriented at 25° at zero overtravel. The vertical overtravel was imposed on the cantilever by using the adjustable laboratory support—in this setup the overtravel accuracy was determined to be ±0.5mm. A suitably-positioned digital camera was used to verify the roll error angle φ and to ascertain when contact planarity was achieved. This setup was also used to determine the contact force versus overtravel relationship of all cantilevers. The experiments were performed several times to ensure repeatability.

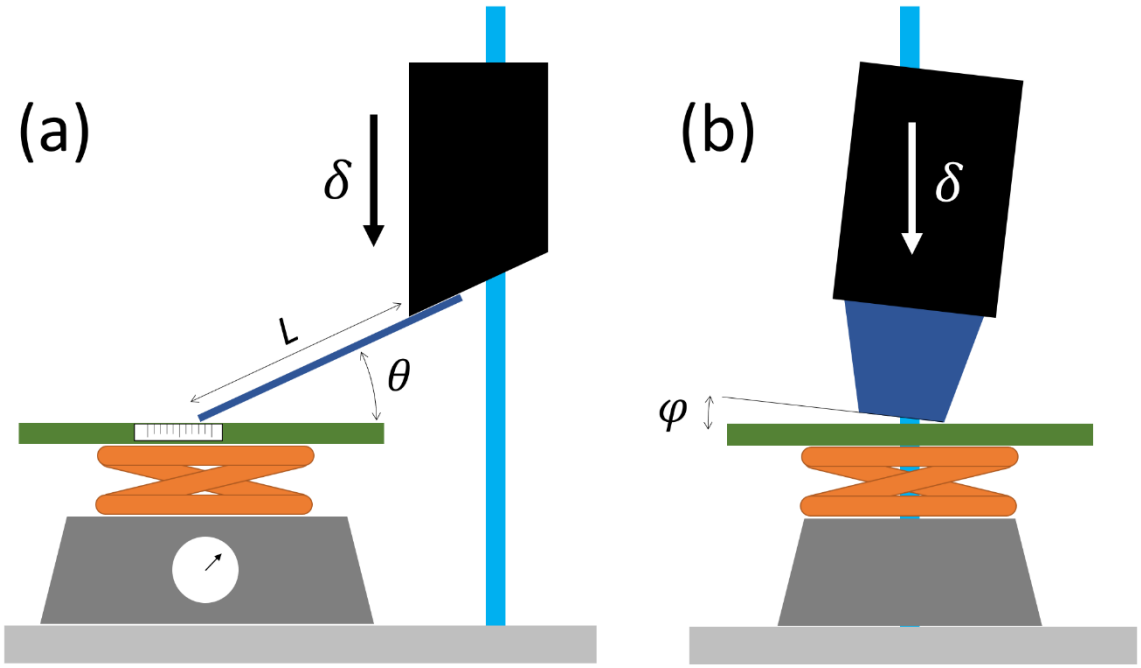

Figure 9. Schematic diagram of experimental setup used to determine the contact force at cantilever tip planarity versus roll error. (a) Side view and (b) end view. The arrows indicate the direction of the overtravel. The cantilever (blue) is attached to a sliding mechanical part (black) which is mounted onto a laboratory stand (light blue). The mechanical part enables the cantilever tilt angle θ to be fixed at 25°. A roll error angle φ is imposed on the cantilever. The overtravel is imposed and the apex of the cantilever skates across the surface (green) until the apex is planar to the surface. At apex planarity, the contact force is recorded using the precision scales (grey).

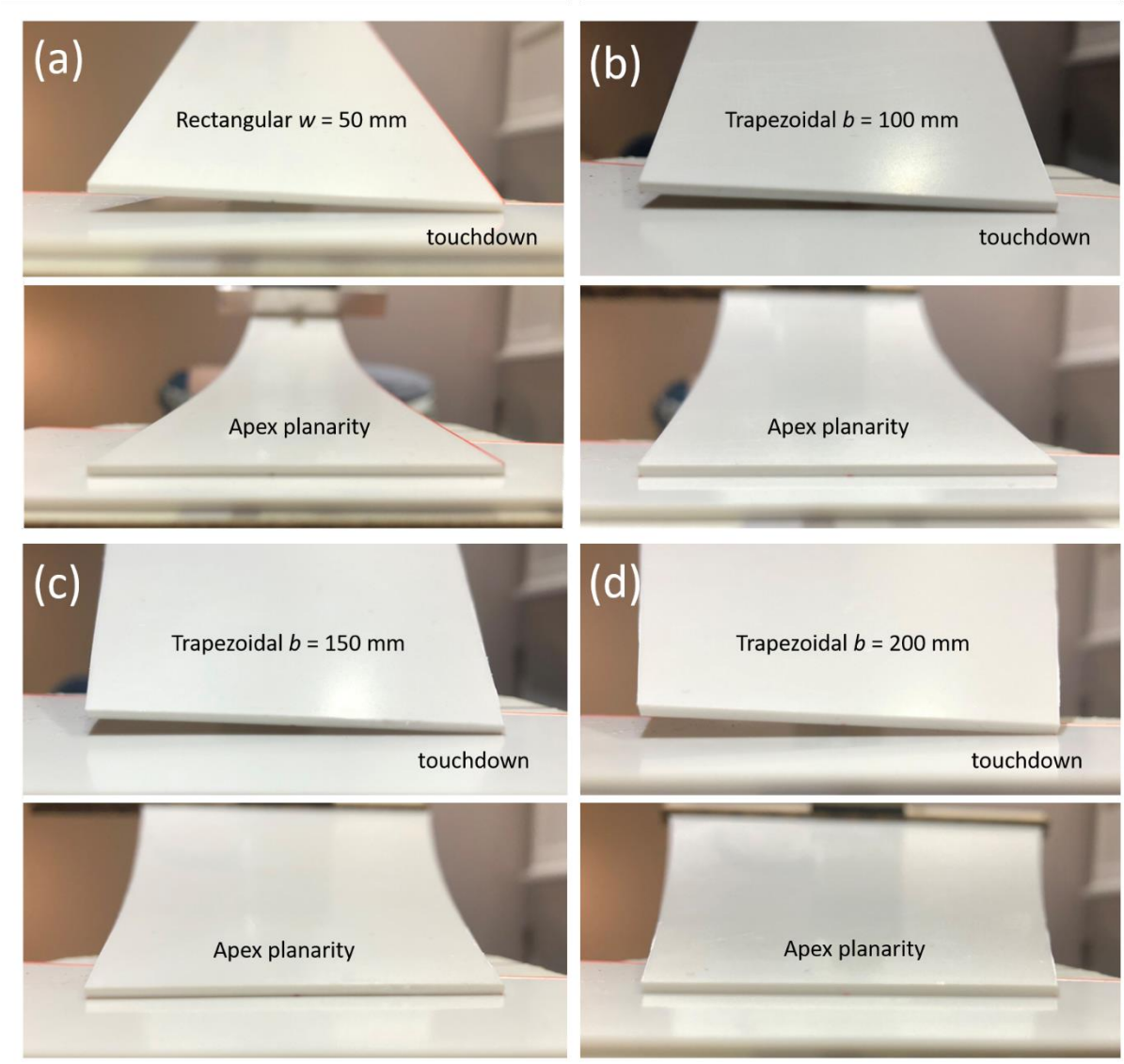

Figure 10. Contact force experimental results. Photographs of cantilever having a roll error angle in touchdown (upper images) and in apex planarity (lower images) for cantilevers having a base width b of (a) 50 mm, (b) 100 mm, (c) 150 mm, and (d) 200 mm. The apex of the cantilevers measures 50 mm, its thickness is 1.5 mm, and its length is 250 mm. The scale bars indicate 10 mm.

Figure 10 shows photographs of the experimental results. Each cantilever was initially brought into contact with the surface (upper images) and an overtravel is imposed until apex planarity was observed (lower images). The contact force at apex planarity was deduced as a function of cantilever base width.

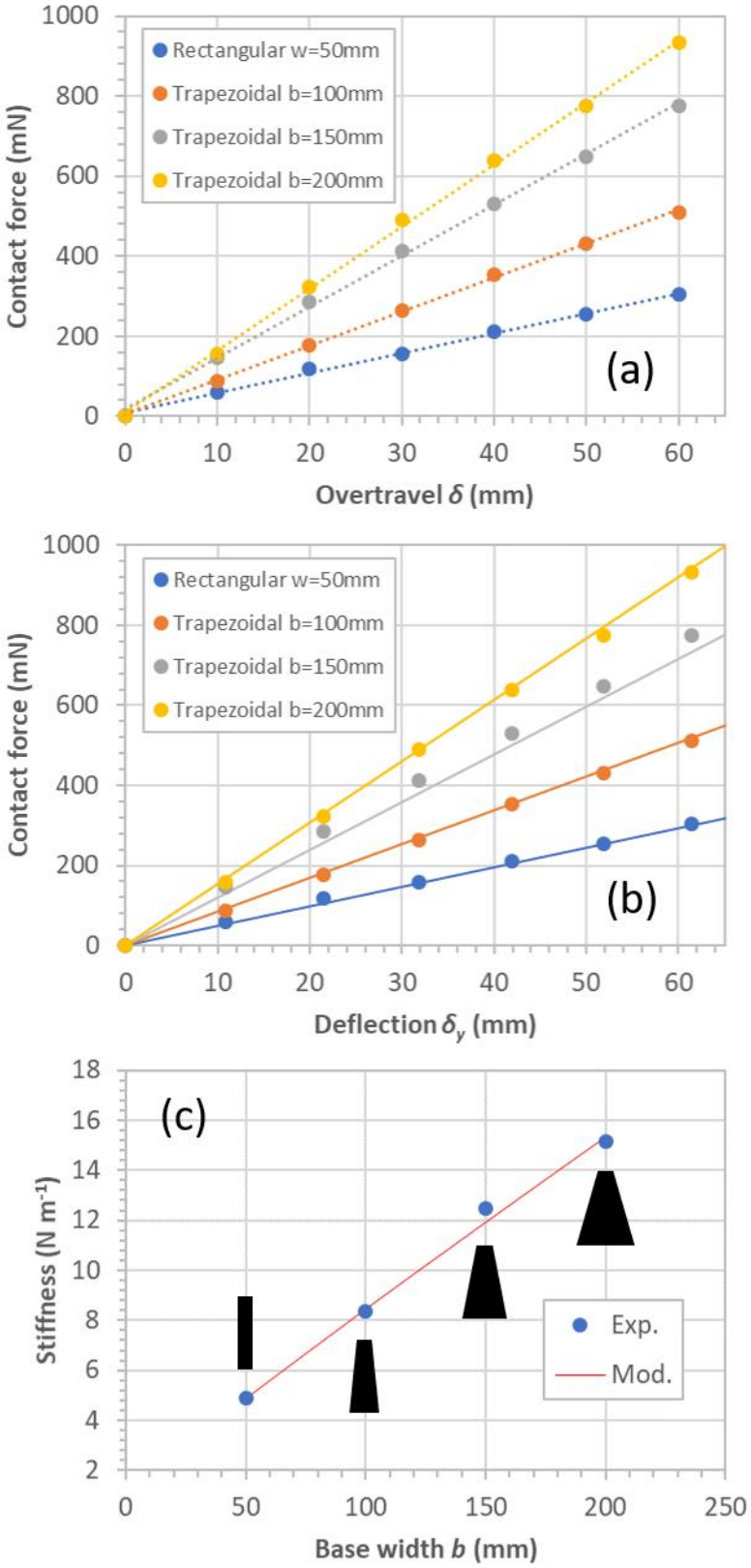

Figure 11. Experimental results. (a) contact force as a function of apex deflection. (b) contact force as a function of overtravel. (c) the cantilever stiffness as a function of cantilever base width b. The dashed

lines in (a) correspond to linear fits of the data. The solid lines in (b) and (c) are solutions of the Euler-Bernoulli equation.

Figure 11 shows plots of the experimental data. First, the contact force increases linearly with overtravel and increases with increasing cantilever base width—Fig. 11(a). The overtravel can be converted to apex deflection using the formulae above—this is plotted in Fig. 11(b). The solid lines in Fig. 11(b) correspond to Equation 13 above, the data fits the theory very well. The slopes of the data in Fig. 11(b) enables the cantilever stiffnesses to be deduced—this is plotted in Fig. 11(c) and corresponds very well with modelling. The trapezoidal cantilever is 2% stiffer than it should be, but as the stiffness varies as t^3/L^3, the maximum dimension errors: 0.5 mm for L and 0.012 mm for t, can account for this small discrepancy.

The experiments using the rectangular cantilever enabled the elastic modulus of the polystyrene sheets used here to be determined to be 1.754±0.071 GPa. This value falls in the range of published values for 'dense polystyrene' 1.6-3.4 GPa, e.g. Cheng *et al* [28] reported a value of 1.6 GPa and 1.8 GPa using two different indentation methods. Valentova and Stejskal reported 1.8 GPa [29], Miyake *et al* [30] measured a value of 2.3 GPa using AFM nanoindentation methods. The value for bulk, very dense polystyrene is reported to be in the range 3.2-3.4 GPa [23].

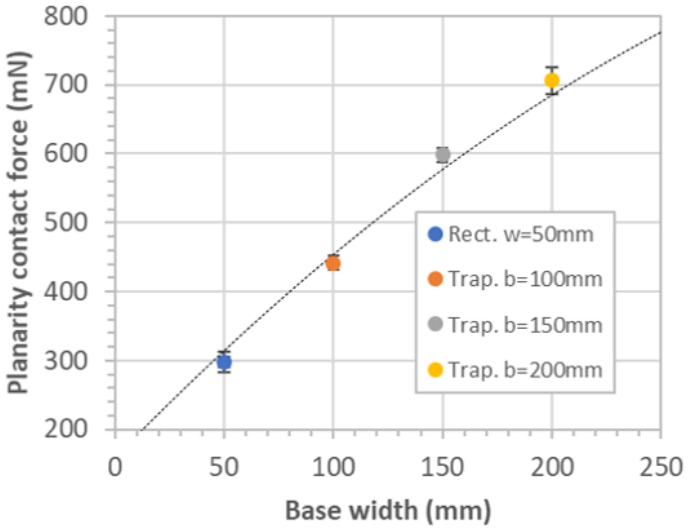

Figure 12. Experimental results and comparison with modelling. The planarity experimentally-determined contact force (filled circles) as a function of cantilever base width. The dashed black curve is the result of the modelling.

Figure 12 plots the experimentally-obtained contact force (filled circles) required to achieve apex planarity for four cantilever of varying base width b. In this case the roll error angle was 3°. The planarity contact force increases with increasing base width. The dashed black line shows the result of the modelling. This is the best fit of the modelling to the experimental data by using a Poisson's ratio of 0.33. For dense polystyrene, Hughes *et al* [31] reported a Poisson's ratio of 0.336. A Poisson's ratio equal to 0.33 enabled a reasonable fit of the experimental data to the model. This enables the value of the shear modulus to be determined to be 659.4 MPa. These values are in comparable with accepted published values [32] for dense polystyrene and indicates that the model works well.

Let us now consider some practical issues of MEMS-based electrical probes where the above findings are of some relevance.

6. Compensating for roll error

This section discusses three methods of roll error compensation in a flexible microcantilever-based electrical probe having two or more contacts. First, mechanical torsion of the cantilever can be used to bring the whole of the apex of the probe into contact with the surface. In this case an overtravel will be necessary to achieve a requited contact force on all contact pads. Second, two cases of probe rotation compensation of roll error are considered. These are the case where a fine control of the roll angle is possible, and the case where the contact pads do not contact with the substrate on touchdown.

6.1 Torsional compensation for roll error

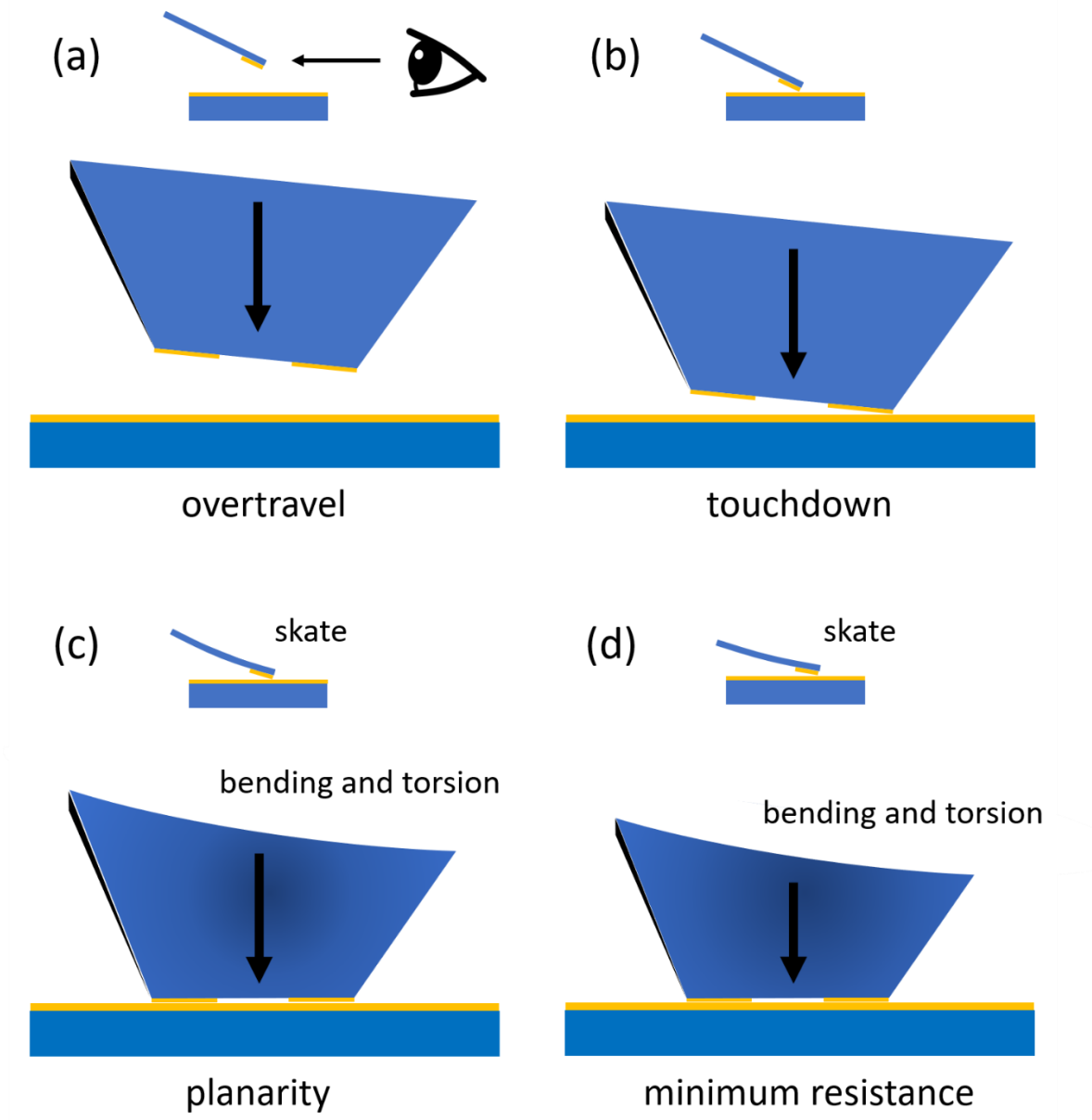

Figure 13. Schematic diagram showing torsional compensation of roll error angle in a flexible microcantilever-based probe. (a) Vertical downward overtravel. (b) Touchdown of right-hand contact pad with surface. (c) Further overtravel leads to bending and torsion of the cantilever to achieve apex planarity. (d) Further overtravel increases the contact force to achieve two low resistance contacts. The eye inset to (a) shows how one is looking at the apex of the cantilever in the figure.

Figure 13 shows how the natural torsion of the microcantilever can lead to roll error compensation. This method is useful if the roll angle of the probe cannot be finely controlled and also if the contact pads do not make contact with the surface upon initial probe touchdown.

Initially, the probe is not in contact with the surface—Fig. 13(a). A downward overtravel is imposed to bring one corner of the right-hand contact pad at the apex of the probe into contact with the surface; this is probe touchdown—see Fig. 13(b). At this point an electrical resistance is perhaps measurable. The left-hand contact pad of the probe is not in contact with the surface—it is a distance of $a \sin \varphi$ above the surface. At this point the cantilever is not bending and the contact force is zero. Further downward overtravel is imposed to the probe—see Fig. 13(c). When the left-hand probe pad enters into contact with the surface due to bending and torsion, an electrical resistance will be measurable. At this point the planarity overtravel is known. By using Equation 20 above, the value of the roll error angle is also known. The probe apex has also skated across the surface, the value of which can be calculated by the model. The contact force between the right-hand-side pad and the surface is greater than zero and given by the model. Next, if further downward overtravel is imposed, several things happen—see Fig. 13(d). First, the cantilever bends more. Second, the tip skates further across the surface. Third, the contact force increases on both the left-hand and the right-hand pads. This results in a reduction of the contact resistance between the pads and the surface. The overtravel can be increased until the left-hand pad contact force is sufficient to minimize the contact resistance.

6.2 Rotational correction for roll error angle

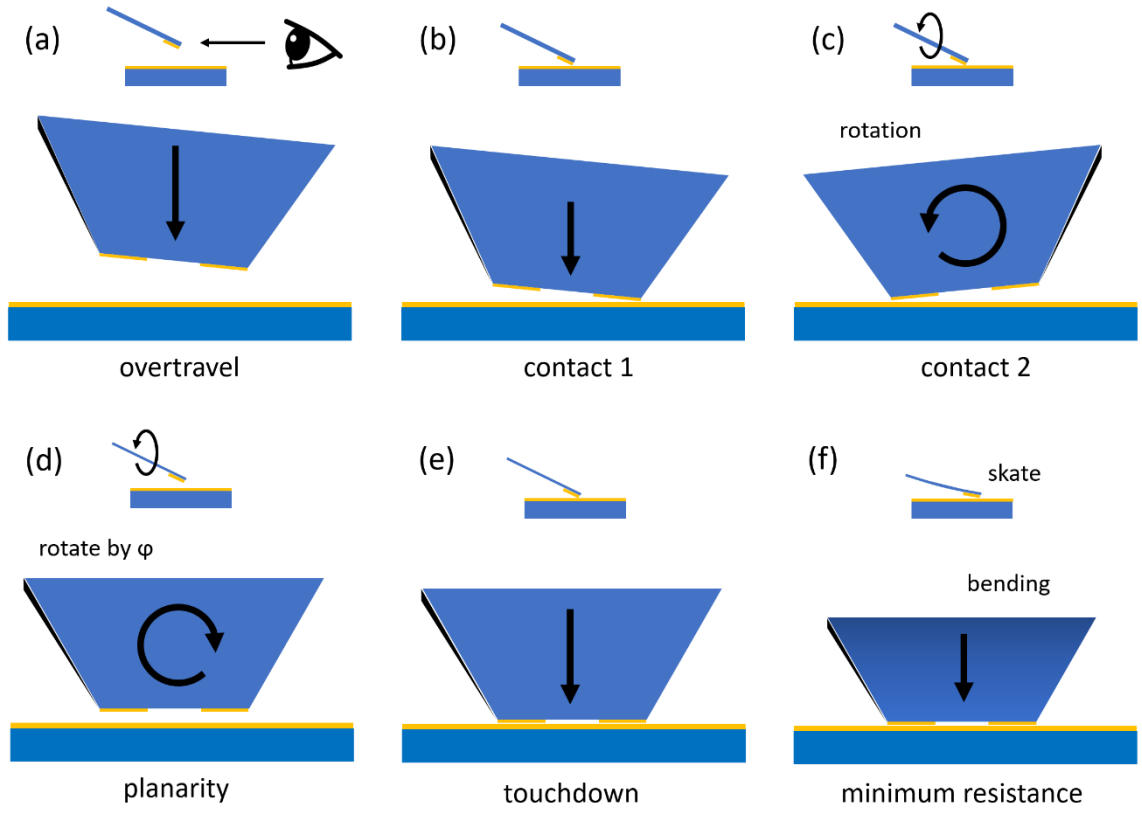

Figure 14. Schematic diagram showing roll error angle correction if contact pads make electrical contact upon touchdown. a) Vertical downward overtravel. (b) Touchdown of right-hand contact pad with surface. (c) rotation of probe to make left-hand contact with surface. (d) reverse rotation by an angle of φ to achieve planarity. (e) Downward overtravel to achieve touchdown. (f) Further overtravel increases the contact force to achieve two low resistance contacts.

Figure 14 shows a trivial solution for roll error angle correction in a microcantilever-based probe if: (i) the metalized contact pads make contact with the surface on initial touchdown and (ii) the roll angle of the probe can be accurately controlled. In this case probe touchdown is made by imposing overtravel—Fig. 14(b). The probe is rotated until the other pad makes electrical contact with the underlying surface—Fig. 14(c). This rotation corresponds to 2φ degrees. The probe is then reverse rotated by φ degrees—see Fig. 14(d)—to achieve apex planarity. Further overtravel is then imposed to achieve touchdown—Fig. 14(e)—and minimum contact resistance—Fig. 14(f)—via bending of the cantilever and resulting skate [22,23]. The Supplementary Information shows a figure for the trivial case of a rigid commercial probe.

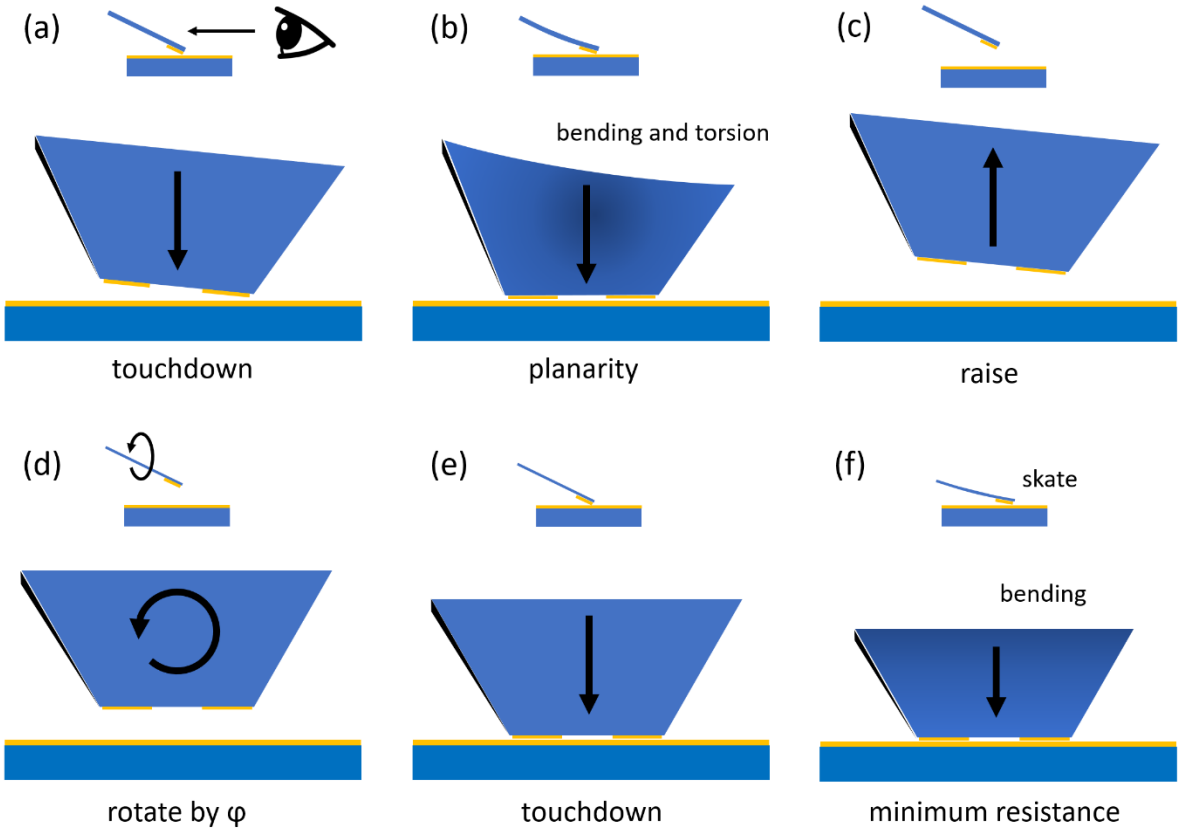

Figure 15. Schematic diagram of roll error angle correction if contact pads do not make electrical contact upon initial touchdown. (a) Downward overtravel achieves touchdown and (b) planarity of the apex of the probe. (c) the probe is raised and (d) rotated by φ to achieve apex planarity. (e) downward overtravel achieves touchdown with planarity. (f) further overtravel achieves minimum contact resistance on both pads.

Figure 15 shows a protocol for roll error angle correction if, due to design or fabrication constraints, the metallized contacts do not make contact with the surface upon initial touchdown. Again, an overtravel brings the probe into touchdown—Fig. 15(a). Further overtravel is then imposed to achieve apex planarity—Fig. 15(b). Here, two contact resistance are measurable. Knowing the value of the overtravel enables the roll error angle to be computed. The probe can then be raised and rotated by φ degrees to achieve apex planarity—Fig. 15(d). A downward overtravel can now be applied to the probe to bring the two probe pads simultaneously into contact with the surface; this is probe touchdown—Fig. 15(e). Here the cantilever is not bending and contact force on both pads is zero. Further downward overtravel can now be applied to the probe—Fig. 15(f). The effect of this is to cause the probe apex to skate over the surface by a known amount given by the model. In addition, the contact force between the probe pads and the surface can be increased until a minimum contact

resistance is achieved. In the case of miniature probes, rotational compensation of the probe may simply not be possible due to the required resolution of the roll angle control. Let us consider a pad metallization thickness m at a distance g from the edge of the cantilever. In this case if the roll error angle is greater than $\tan^{-1} m/g$ then the pad will not be in electrical contact with the surface upon probe touchdown.

7. The practical example of a silicon microcantilever-based probe

Let us now consider specific practical examples where all this could be of some use. Consider two flexible trapezoidal-shaped silicon microcantilever-based probes having 2 electrical contact pads—as shown in Figure 16. In both cases, the cantilever has a length of 200 µm, an apex length of 15 µm, and a thickness of 5 µm. Probe 1 has a base width of 200 µm and probe 2 has a base width of 50 µm. The microcantilevers are supported by a thick millimetre-sized silicon support chip. In the current examples we will consider the gold thickness to be much less than the cantilever thickness, e.g. 100 nm, meaning: (i) potential mechanical damage of the gold pads [20,21] is not considered in a first approximation and (ii) the properties of the gold have negligible mechanical impact on the cantilever. The cantilevers are fabricated on a (100) silicon wafer and the cantilevers lengths are oriented in the [011] crystal direction. In this case, the Poisson's ratio of silicon is 0.065 [33]. The elastic modulus of silicon for this direction [011] is 169 GPa [26], therefore the shear modulus is 79 GPa.

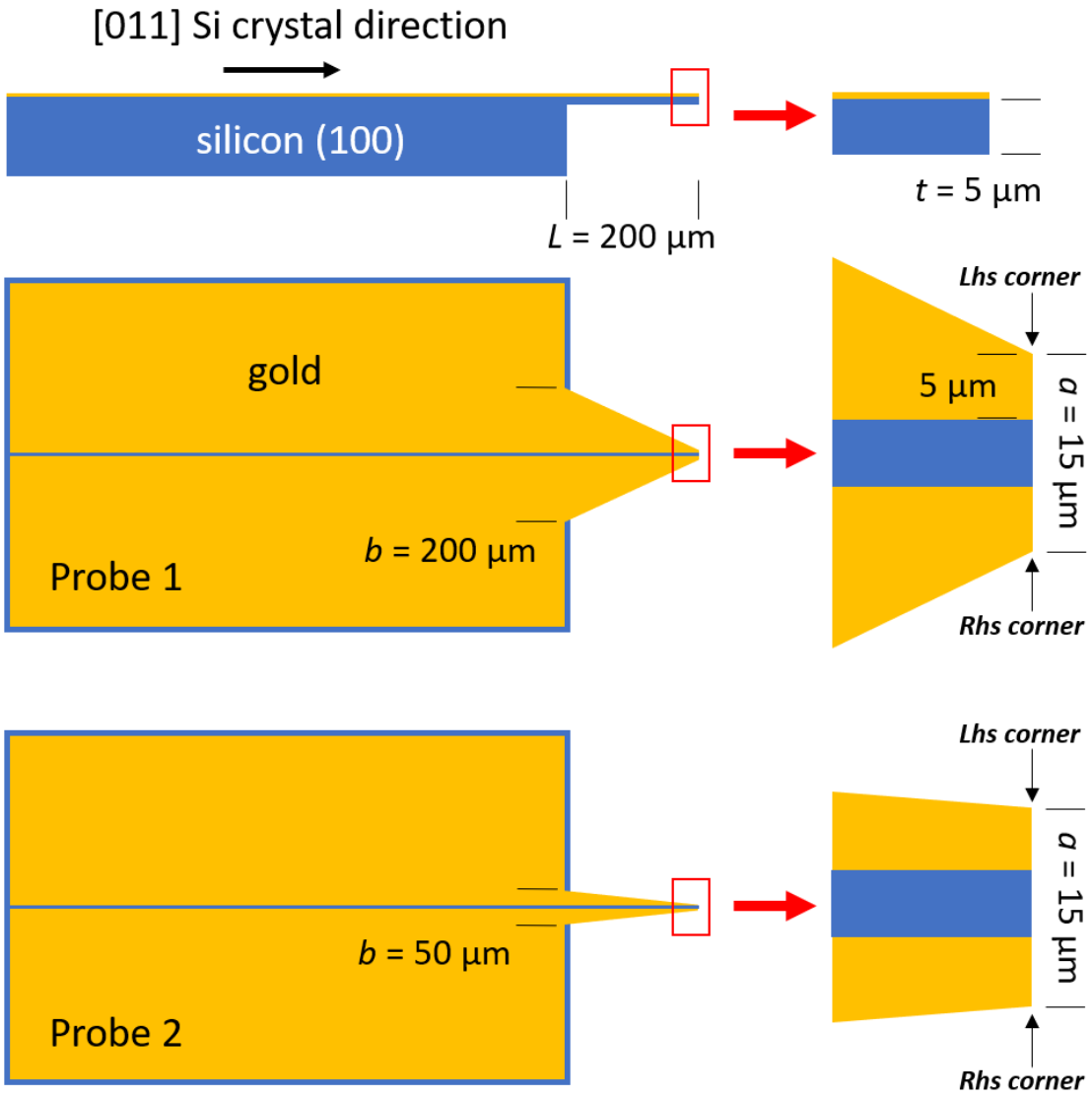

Figure 16. Two MEMS-based two-contact probes employing a flexible trapezoidal-shaped silicon microcantilever. The right-hand side corner and left-hand side corner of the probes are indicated in the figure.

Let us assume we are trying to achieve two low-resistance electrical contacts onto an underlying flat metal surface—this could be the electrical contacts of a device targeted for testing. The probe is oriented at a tilt angle of 25° relative to the flat underlying surface. As the goal is to have two low resistance contacts, e.g. <1Ω. In order to do so, we assume that a minimum contact force of 400 µN is required for each contact [21]. Let us also consider that the unknown roll error angle φ is smaller than the resolution of the support rotation mechanism. This means that a simple roll error correction described above could be problematic. We will therefore use the torsional compensation approach also described above.

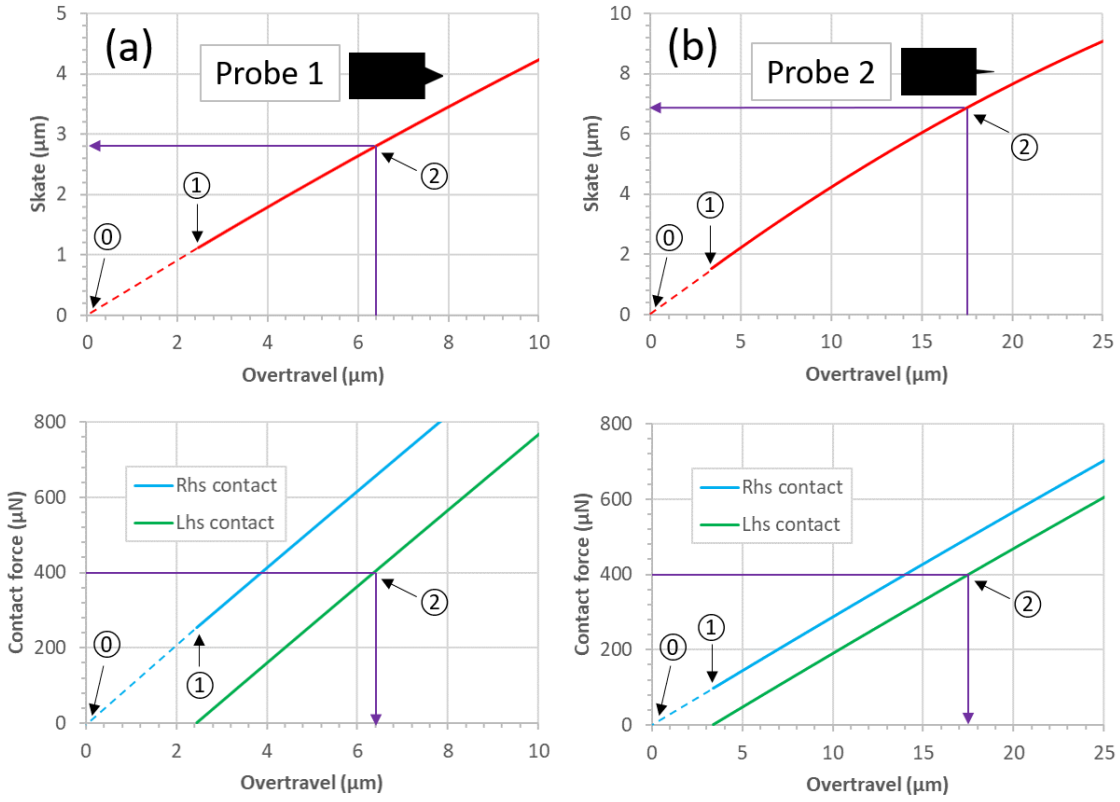

Figure 17. Results of the modelling of two microcantilever-based probes. (a) Probe 1 ($b = 200\ \mu m$); skate versus overtravel (upper image) and contact force versus overtravel (lower image). (b) Probe 2 ($b = 50\ \mu m$); skate versus overtravel (upper image) and contact force versus overtravel (lower image). The points ⓪ correspond to touchdown of one corner of the apex of the probe. The points ① correspond to apex planarity where the probe apex is planar to the underlying surface. The points ② corresponds to when enough excess overtravel has been applied to increase the contact force of the left-hand apex corner to the required value to a low resistance contact—400 µN in this case. Rhs = corresponds to right-hand side, Lhs corresponds to left-hand side.

With reference to Figure 17, let us first consider probe 1 ($b = 200\ \mu m$). First, we lower the probe until the right-hand corner of the tip apex makes electrical contact with the surface. This is the zero overtravel point ⓪, the origin on the graphs shown in Fig. 17(a). Next, the overtravel is gradually increased and noted. At point ① in Fig. 17(a) the apex of probe 1 is now planar to the surface. We know this as both electrical contacts are conducting. The overtravel to achieve this is measured to be 2.46 µm. The apex skate at this point is therefore 1.12 µm, calculated via the modelling. The contact

force of the right-hand side corner is calculated to be 253.2 µN. At this point the modelling allows us to compute the roll error angle to be 0.1°. We are now able to increase the overtravel to achieve a required contact for of 400 µN on both contacts. At point ② in Fig. 17(a) the overtravel has been increased to 6.38 µm (computed by the model) to create a contact force of 400 µN on the left-hand side corner of the apex. The contact force on the right-hand side corner is now 653.2 µN and the apex skate is 2.80 µm—also computed by the model. At this point we should measure two low resistance electrical contacts between the probe and the surface.

Now, with reference again to Figure 17, let us now consider probe 2 ($b = 50\ \mu m$). First, we lower the probe until the right-hand corner of the tip apex makes electrical contact with the surface. This is the zero overtravel point ⓪, the origin on the graphs shown in Fig. 17(b). Again, the overtravel is gradually increased and noted. At point ① in Fig. 17(b) the apex of probe 2 is now planar to the surface. We know this as both electrical contacts are conducting. The overtravel to achieve this is measured to be 3.36 µm. The apex skate at this point is therefore 1.52 µm, calculated via the modelling. The contact force of the right-hand side corner is calculated to be 97.9 µN. At this point the modelling allows us to compute the roll error angle to be 0.1°. We are now able to increase the overtravel to achieve a required contact for of 400 µN on both contacts. At point ② in Fig. 17(a) the overtravel has been increased to 17.51 µm (computed by the model) to create a contact force of 400 µN on the left-hand side corner of the apex. The contact force on the right-hand side corner is now 497.9 µN and the apex skate is 6.88 µm—also computed by the model. At this point we should measure two low resistance electrical contacts between the probe and the surface.

One can consider the importance of friction in the skating (forward and lateral) in sliding electrical contacts. The situation is complicated by many issues such as force depended friction, cycling, and damage [34]. In the example above of gold-on-gold, the friction coefficient of gold-on-gold is reported to be both force depended and cycle-dependent [35]: a value of 0.14 is reported for low forces meaning skate should occur. It is well known that probe skating can cause damage to probe contacts and pad metals. As a practical solution to skate-induced damage, I have previously proposed a zero-skate solution in which friction is irrelevant and tip/pad damage would be reduced [22,23].

Finally, the author notes that the integration of stress sensors, e.g. using piezoresistors [36], enables bending to be measured electrically and also gives knowledge of bending stress to avoid failure due to fracture.

8. Impact of pitch error on the modelling of the probes.

Finally, the model an also be used to evaluate the impact of the pitch error—commonly referred to as 'tilt error'. let us now see the effect of the pitch error on these results.

	$\boldsymbol{\theta = 24°}$	$\boldsymbol{\theta = 25°}$	$\boldsymbol{\theta = 26°}$
$\boldsymbol{\delta_p}$ (μm)	2.48	2.46	2.44
$\Delta_{\boldsymbol{p}}$ (μm)	1.08	1.12	1.16
$\boldsymbol{\delta_{fc}}$ (μm)	6.43	6.38	6.33
$\Delta_{\boldsymbol{fc}}$ (μm)	2.69	2.80	2.91

Table 1. Impact of pitch error on the modelling of probe 1 (b = 200 μm). δ_p is the overtravel required for apex planarity, Δ_p is the skate at planarity, δ_{fc} is the overtravel required to achieve enough contact force for a low resistance contact (400 μN for the modelling), and Δ_{fc} is the resulting skate.

	$\boldsymbol{\theta = 24°}$	$\boldsymbol{\theta = 25°}$	$\boldsymbol{\theta = 26°}$
$\boldsymbol{\delta_p}$ (μm)	3.39	3.36	3.34
$\Delta_{\boldsymbol{p}}$ (μm)	1.46	1.52	1.56
$\boldsymbol{\delta_{fc}}$ (μm)	17.63	17.51	17.39
$\Delta_{\boldsymbol{fc}}$ (μm)	6.57	6.88	7.18

Table 2. Impact of pitch error on the modelling of probe 2 (b = 50 μm). δ_p is the overtravel required for apex planarity, Δ_p is the skate at planarity, δ_{fc} is the overtravel required to achieve enough contact force for a low resistance contact (400 μN for the modelling), and Δ_{fc} is the resulting skate.

We can compare Tables 1 and 2. The main conclusions from this are First the pitch error will modify the ultimate overtravel required for a correct contact force. A larger angle resulting in a higher skate. Second, pitch error will have a greater consequence in less stiff MEMS. We can see this from Table 2 where the skate increases by 600 nm from a tilt angle of 24° to a tilt angle of 26°.

9. Conclusions

Analytical modelling can describe roll angle position error in microelectromechanical systems (MEMS) based probes having two or more electrical contact pads. By taking into consideration the bending, the torsion, the tip skate, and the contact force of a given cantilever, elegant equations relating the

overtravel required for apex planarity are derived. Interestingly, these equations involve only the Poisson's ratio of the cantilever material, not the absolute values of the elastic or shear moduli. For a given roll error angle, the model can predict the overtravel required to achieve probe tip planarity. The model also predicts the contact force on each contact pad—and, in principle, can be used to anticipate the impact of roll error angle on the quality of electrical contact testing. The model can be tested using centimetre-sized cantilevers. This approach is easier than the more-challenging characterization of miniature microcantilevers. The methodology of the measurements and the modelling enables the mechanical properties (elastic modulus, shear modulus, and Poisson's ratio) of the material to be evaluated. The predictions of the modelling agree reasonably well with the experimental findings. As the model is scalable, one can conclude that, at least in principle, it can be used in a first approximation to understand roll angle positioning errors in miniature MEMS-based probes based on silicon microcantilevers. The findings have permitted protocols for the compensation and correction of roll error in flexible microcantilever-based probes to be suggested. A flexible microcantilever enables a torsional compensation of the roll error angle. It also enables the roll error angle to be corrected. The specific geometry of the probe tip and experimental setup will determine which approach is best suited. It is hoped that the ideas and findings presented here are useful for the test engineer and the designer of MEMS probes being potentially used for automated probing.

Acknowledgements

The author would like to thank Jean-Michel Mallet for the fabrication of the mechanical cantilever holder used for the overtravel/skate/torsion experiments. The work was carried out in support of the French ANR project PRECISE.

[1] Strid E 1997 A History of Microwave Wafer Probing *50th ARFTG Conference Digest* 50th ARFTG Conference Digest (Portland, OR, USA: IEEE) pp 27–34

[2] Wartenberg S A 2003 Selected topics in rf coplanar probing *IEEE Trans. Microw. Theory Tech.* **51** 1413–21

[3] Rumiantsev A and Doerner R 2013 RF Probe Technology: History and Selected Topics *IEEE Microw. Mag.* **14** 46–58

[4] Sakamaki R and Horibe M 2021 Investigation on practical problems in on-wafer measurement for actual devices *2021 97th ARFTG Microwave Measurement Conference (ARFTG)* 2021 97th ARFTG Microwave Measurement Conference (ARFTG) (Atlanta, GA, USA: IEEE) pp 1–3

[5] Wu W, Liu B, He P, Wen X, Yang H, Cao Y, Wang Z, Shi G, Yang Q, Zhang A and Guo C 2022 A W-Band GSG Probe Fabricated by Metal Additive Manufacturing *IEEE Trans. Instrum. Meas.* **71** 1–10

[6] Fisher, G A 2015 A guide to successful on wafer RF characterisation (Cascade Microtech Europe Ltd).

[7] Atasoy H, Unlu M, Topalli K, Istanbulluoglu I, Temocin E U, Bayraktar O, Demir S, Civi O, Koc S and Akin T 2006 Investigation of On-Wafer TRL Calibration Accuracy Dependence on Transitions and Probe Positioning *2006 European Microwave Conference* 2006 European Microwave Conference (Manchester, UK: IEEE) pp 1582–5

[8] Phung G N, Schmuckle F J, Doerner R, Kahne B, Fritzsch T, Arz U and Heinrich W 2019 Influence of Microwave Probes on Calibrated On-Wafer Measurements *IEEE Trans. Microw. Theory Tech.* **67** 1892–900

[9] Chen L, Zhang C, Reck T J, Arsenovic A, Bauwens M, Groppi C, Lichtenberger A W, Weikle R M and Barker N S 2012 Terahertz Micromachined On-Wafer Probes: Repeatability and Reliability *IEEE Trans. Microw. Theory Tech.* **60** 2894–902

[10] Phung G N and Arz U 2020 Parasitic Probe Effects in Measurements of Coplanar Waveguides with Narrow Ground Width *2020 IEEE 24th Workshop on Signal and Power Integrity (SPI)* 2020 IEEE 24th Workshop on Signal and Power Integrity (SPI) (Cologne, Germany: IEEE) pp 1–4

[11] Yu Q, Bauwens M F, Zhang C, Lichtenberger A W, Weikle R M and Barker N S 2013 Improved Micromachined Terahertz On-Wafer Probe Using Integrated Strain Sensor *IEEE Trans. Microw. Theory Tech.* **61** 4613–20

[12] Sakamaki R and Horibe M 2020 Precision Adjustment of Probe Tilt Angle with RF Signal Detection Technique *IEEE Trans. Instrum. Meas.* 1–1

[13] Sakamaki R and Horibe M 2018 Proposal of a Precision Probe-Tilt Adjustment with the RF Signal Detection Technique *2018 Conference on Precision Electromagnetic Measurements (CPEM 2018)* 2018 Conference on Precision Electromagnetic Measurements (CPEM 2018) (Paris: IEEE) pp 1–2

[14] Sakamaki R and Horibe M 2022 In-situ automatic adjustment of probe positions and tilt angles for GSGSG probe *2021 51st European Microwave Conference (EuMC)* 2021 51st European Microwave Conference (EuMC) (London, United Kingdom: IEEE) pp 789–92

[15] El Fellahi A, Haddadi K, Marzouk J, Arscott S, Boyaval C, Lasri T and Dambrine G 2015 Nanorobotic RF probe station for calibrated on-wafer measurements *2015 European Microwave Conference (EuMC)* 2015 European Microwave Conference (EuMC 2015) (Paris, France: IEEE) pp 163–6

[16] Daffe K, Marzouk J, Fellahi A E, Xu T, Boyaval C, Eliet S, Grandidier B, Arscott S, Dambrine G and Haddadi K 2017 Nano-probing station incorporating MEMS probes for 1D device RF on-wafer characterization *2017 47th European Microwave Conference (EuMC)* 2017 47th European Microwave Conference (EuMC) (Nuremberg: IEEE) pp 831–4

[17] Taleb A, Pomorski D, Boyaval C, Arscott S, Dambrine G and Haddadi K 2020 Control and Automation for Miniaturized Microwave GSG Nanoprobing *Machine Vision and Navigation* ed O Sergiyenko, W Flores-Fuentes and P Mercorelli (Cham: Springer International Publishing) pp 751–68

[18] Reck T J, Chen L, Zhang C, Arsenovic A, Groppi C, Lichtenberger A W, Weikle R M and Barker N S 2011 Micromachined Probes for Submillimeter-Wave On-Wafer Measurements—Part I: Mechanical Design and Characterization *IEEE Trans. Terahertz Sci. Technol.* **1** 349–56

[19] Reck T J, Chen L, Zhang C, Arsenovic A, Groppi C, Lichtenberger A, Weikle R M and Barker N S 2011 Micromachined Probes for Submillimeter-Wave On-Wafer Measurements—Part II: RF Design and Characterization *IEEE Trans. Terahertz Sci. Technol.* **1** 357–63

[20] Marzouk J, Arscott S, Fellahi A E, Haddadi K, Lasri T, Christophe Boyaval and Dambrine G 2015 MEMS probes for on-wafer RF microwave characterization of future microelectronics: design, fabrication and characterization *J Micromech Microeng* **25** 075024

[21] Daffe K, Marzouk J, Boyaval C, Dambrine G, Haddadi K and Arscott S 2022 A comparison of pad metallization in miniaturized microfabricated silicon microcantilever-based wafer probes for low contact force low skate on-wafer measurements *J. Micromechanics Microengineering* **32** 015007

[22] Arscott S 2022 On overtravel and skate in cantilever-based probes for on-wafer measurements *J. Micromechanics Microengineering* **32** 057001

[23] Arscott S 2022 Skate, overtravel, and contact force of tilted triangular cantilevers for microcantilever-based MEMS probe technologies *Sci. Rep.* **12** 19386

[24] Timoshenko S 2010 *Theory of elasticity* (New Delhi, India: McGraw-Hill Education)

[25] Young W C and Budynas R G 2002 *Roark's formulas for stress and strain* (New York: McGraw-Hill)

[26] Hopcroft M A, Nix W D and Kenny T W 2010 What is the Young's Modulus of Silicon? *J. Microelectromechanical Syst.* **19** 229–38

[27] Vaziri M, Stott F H and Spurr R T 1988 Studies of the friction of polymeric materials *Wear* **122** 313–27

[28] Cheng L, Xia X, Yu W, Scriven L E and Gerberich W W 2000 Flat-punch indentation of viscoelastic material *J. Polym. Sci. Part B Polym. Phys.* **38** 10–22

[29] Valentová H and Stejskal J 2010 Mechanical properties of polyaniline *Synth. Met.* **160** 832–4

[30] Miyake K, Satomi N and Sasaki S 2006 Elastic modulus of polystyrene film from near surface to bulk measured by nanoindentation using atomic force microscopy *Appl. Phys. Lett.* **89** 031925

[31] Hughes D S, Blankenship E B and Mims R L 1950 Variation of Elastic Moduli and Wave Velocity with Pressure and Temperature in Plastics *J. Appl. Phys.* **21** 294–7

[32] Brandrup J, Immergut E H, Grulke E A, Abe A and Bloch D R 1999 *Polymer handbook* (Hoboken, N. J: Wiley)

[33] Wortman J J and Evans R A 1965 Young's Modulus, Shear Modulus, and Poisson's Ratio in Silicon and Germanium *J. Appl. Phys.* **36** 153–6

[34] Chandross M and Argibay N 2021 Friction of Metals: A Review of Microstructural Evolution and Nanoscale Phenomena in Shearing Contacts *Tribol. Lett.* **69** 119

[35] Beake B D, Harris A J, Liskiewicz T W, Wagner J, McMaster S J, Goodes S R, Neville A and Zhang L 2021 Friction and electrical contact resistance in reciprocating nano-scale wear testing of metallic materials *Wear* **474–475** 203866

[36] Peiner E and Doering L 2010 MEMS cantilever sensor for non-destructive metrology within high-aspect-ratio micro holes *Microsyst. Technol.* **16** 1259–68